

# Inverse-Designed Metaphotonics for Hypersensitive Detection

Maxim Elizarov, Yuri S. Kivshar, and Andrea Fratallocchi\*

Cite This: *ACS Nanosci. Au* 2022, 2, 422–432

Read Online

ACCESS |

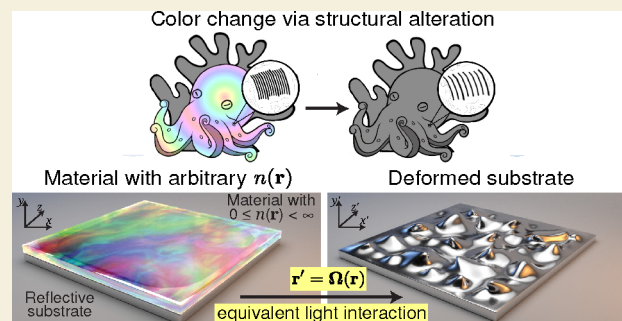
Metrics &amp; More

Article Recommendations

Supporting Information

**ABSTRACT:** Controlling the flow of broadband electromagnetic energy at the nanoscale remains a critical challenge in optoelectronics. Surface plasmon polaritons (or plasmons) provide subwavelength localization of light but are affected by significant losses. On the contrary, dielectrics lack a sufficiently robust response in the visible to trap photons similar to metallic structures. Overcoming these limitations appears elusive. Here we demonstrate that addressing this problem is possible if we employ a novel approach based on suitably deformed reflective metaphotonic structures. The complex geometrical shape engineered in these reflectors emulates nondispersive index responses, which can be inverse-designed following arbitrary form factors. We discuss the realization of essential components such as resonators with an ultrahigh refractive index of  $n = 100$  in diverse profiles. These structures support the localization of light in the form of bound states in the continuum (BIC), fully localized in air, in a platform in which all refractive index regions are physically accessible. We discuss our approach to sensing applications, designing a class of sensors where the analyte directly contacts areas of ultrahigh refractive index. Leveraging this feature, we report an optical sensor with sensitivity two times higher than the closest competitor with a similar micrometer footprint. Inversely designed reflective metaphotonics offers a flexible technology for controlling broadband light, supporting optoelectronics' integration with large bandwidths in circuitry with miniaturized footprints.

**KEYWORDS:** metaphotonics, optical sensor, transformation optics, inverse design, refractive index, optical materials



## INTRODUCTION

In applications that exploit the propagation of electromagnetic beams, it is crucial to control broadband fields in small volumes of matter. At gigahertz frequencies, this reduces chip footprint and increases device speed. At optical wavelengths, strongly localized fields provide the key to many significant effects, including low-threshold lasing, efficient nonlinear harmonic generations, high-resolution imaging, highly sensitive detection, low-power communications, enhanced security, and complex wavefront engineering.<sup>1–9</sup> However, despite impressive recent progress in this field, photonics integration still lags behind electronics, which employs now pioneering devices with characteristic scales of 10 nm or less.<sup>10,11</sup>

To trap light at subwavelength scales, one employs a traditional approach based on collective excitations of electrons and electromagnetic waves in metallic resonators supporting hybrid modes described by surface plasmon polaritons. Currently, metals provide the highest degree of light confinement via plasmonic resonance.<sup>12</sup> However, substantial losses at optical wavelengths create a significant challenge to exploiting these materials for advanced applications.<sup>2,13,14</sup>

The recently emerged field of dielectric resonant metaphotonics provides an alternative physical mechanism of light localization via low-order dipole and multipole Mie resonances that support highly efficient nanoresonators and all-dielectric

metasurfaces.<sup>15</sup> This so-called “Mie-tronics” approach<sup>16</sup> successfully demonstrated the suppression of radiative losses of individual dielectric resonators while engineering unique optical modes with high-quality factors facilitating nonlinear effects at the nanoscale.<sup>3</sup>

However, the refractive index  $n$  attainable in the visible frequency range is relatively small (usually  $n < 5$ ), especially compared to the effective refractive index of metals or dielectrics at longer wavelengths. The currently available materials do not allow realizing a large manifold of concepts initially developed for plasmonics and microwave metamaterials, due to either large metallic losses or unavailability of materials with sufficiently large refractive index response at optical wavelengths. This issue presently confines conceptual demonstrations of many metaphotonics ideas at microwave frequencies.<sup>17–19</sup>

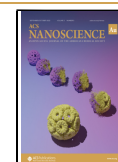
Thus, a novel approach to breaking this limit is highly desirable for implementing many revolutionary ideas with a novel generation of low-loss optical materials and for

Received: February 14, 2022

Revised: June 9, 2022

Accepted: June 9, 2022

Published: July 25, 2022



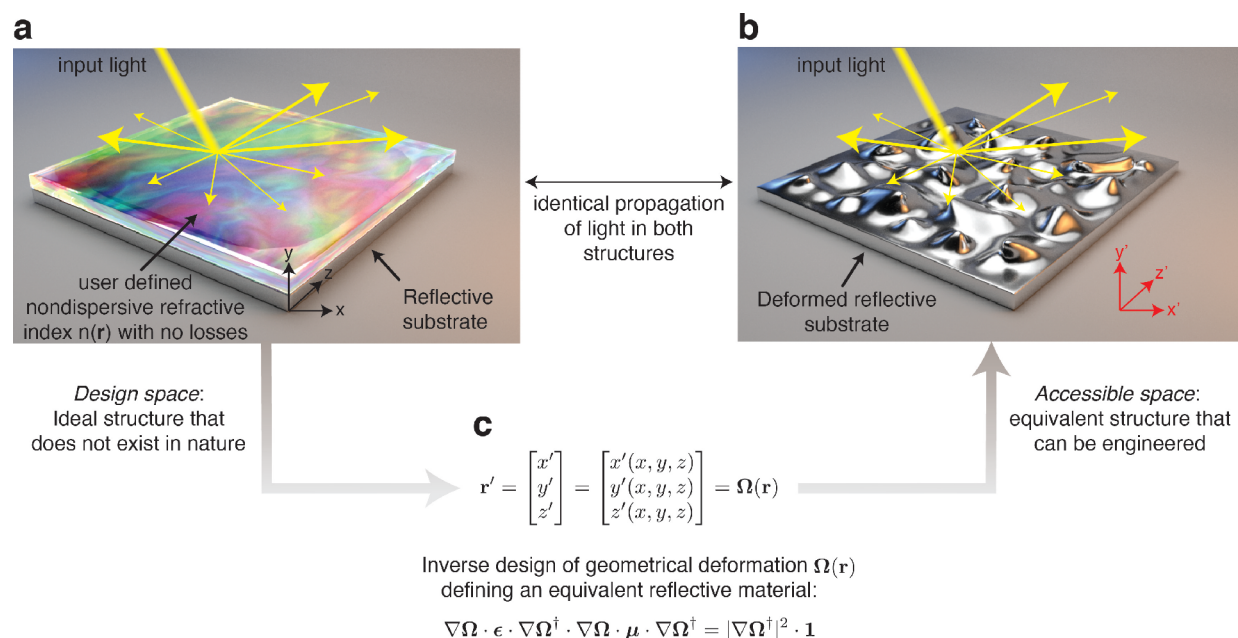


**Figure 1.** Designing materials via geometrical deformations: general principles. (a) Ideal structure for controlling light, characterized by a reflective substrate with a material possessing an arbitrary refractive index distribution on top. (b) Equivalent deformed structure found by inverse design and composed of a reflective substrate in air that possesses the same electromagnetic behavior of (a). (c) Mapping  $\mathbf{r}' = \Omega(\mathbf{r})$  function connecting both domains.

applications of deep subwavelength optics. Here we introduce a novel platform to implement many of those ideas in lossless reflective materials that can help devise many applications. Our approach exploits an inverse design of deformed reflecting structures with user-defined nondispersive refractive indices and spatial form profiles. We discuss basic optical circuitry such as resonators with an ultrahigh refractive index of  $n = 100$  and design a new class of hypersensitive sensors that showed a record value of sensitivity. We believe our approach will provide novel means of strong energy confinement, opening the door to integrated optoelectronic devices with simultaneous control of electrons and photons of large bandwidths in channels of comparable size.

## RESULTS

### Inverse-Designed Materials via Geometrical Deformations

The crucial challenge in controlling light localization at the nanoscale is the quantum mechanical structure of matter combined with reciprocity, representing the intuitive condition that a physical system cannot anticipate the future.<sup>20</sup> Quantum mechanics dictates that the susceptibility response  $\chi(\omega) = n(\omega)^2 - 1$  of any accessible material is a frequency  $\omega$  dependent function combining a series of Lorentz-type resonances (see Chapter 3 of ref 21):

$$\chi(\omega) = \sum_m \left( \frac{a_m}{\omega_m - \omega} + \frac{a_m}{\omega_m^* + \omega} \right) \quad (1)$$

with complex oscillator frequencies  $\omega_m$  and amplitudes  $a_m$ . The causality principle manifests in eq 1 as a rigid relationship, expressed by Kramers–Kronig (KK) relations,<sup>20</sup> between the real and imaginary part of  $\chi(\omega)$ . Due to the direct relationship between  $\chi(\omega)$  and  $n(\omega)$ , KK relations state the impossibility to independently control the real part of  $n(\omega)$ , representing the

effective refractive index of the material, from the material losses, defined by the imaginary part of the refractive index  $n(\omega)$ .

Metallic media possess atomic resonances  $\omega_m$  at visible wavelengths<sup>12</sup> and acquire a strong light localization ability at visible frequencies. However, KK relations constraint high-localization frequencies to points of high absorption, blending the effects of energy localization and losses irreversibly. Dielectric materials, conversely, possess electronic resonances  $\omega_m$  in the deep-blue or ultraviolet frequency range and exhibit transparency over large optical bandwidths. However, the accessible refractive index of these materials in the lossless window is inevitably modest, compromising the resulting localization power, especially if compared to plasmonic media.

Figure 1 shows an alternative material platform that could overcome the issue mentioned above. The starting configuration is a universal basic structure composed by a reflective substrate lying in the  $(x, z)$  plane, with a user-defined, semi-infinite material defined on top (Figure 1a). The medium possesses a nondispersive and lossless anisotropic refractive index  $\mathbf{n}(\mathbf{r}) = \sqrt{\epsilon(\mathbf{r}) \cdot \mu(\mathbf{r})}$ , with  $\epsilon(\mathbf{r})$  and  $\mu(\mathbf{r})$  being the dielectric permittivity and magnetic permeability tensors, respectively, and  $\mathbf{r} = (x, y, z)$  being the position coordinates.

While a material defined as such does not directly exist in nature, we here show that it is possible to engineer this structure by an inverse application of transformation optics.<sup>22–25</sup> Inverse design is a powerful method for creating a material with desired properties<sup>26,27</sup> while transformation optics establishes a relationship between coordinate transformations and geometric materials equivalent to light propagation. Following this correspondence, we wish to implement the user-defined medium  $\mathbf{n}(\mathbf{r})$  from a geometrical deformation of coordinates  $\mathbf{r}' = \Omega(\mathbf{r})$  with

$$\mathbf{r}' = \begin{bmatrix} x' \\ y' \\ z' \end{bmatrix} = \begin{bmatrix} x'(x, y, z) \\ y'(x, y, z) \\ z'(x, y, z) \end{bmatrix} = \Omega(\mathbf{r}) \quad (2)$$

with  $\mathbf{r}'$  transformed coordinates. In the transformed space  $\mathbf{r}'$ , Maxwell equations remain identically the same with the introduction of a new material with dielectric permittivity  $\epsilon'(\mathbf{r}') = \frac{\nabla\Omega \cdot \epsilon \cdot \nabla\Omega^\dagger}{|\nabla\Omega|^2}$  and magnetic permeability  $\mu'(\mathbf{r}') = \frac{\nabla\Omega \cdot \mu \cdot \nabla\Omega^\dagger}{|\nabla\Omega|^2}$  with  $\nabla\Omega = \frac{\partial \mathbf{r}'}{\partial \mathbf{r}}$  the Jacobian matrix.<sup>23</sup> Light cannot differentiate between the materials  $\mathbf{n}(\mathbf{r})$  and  $\mathbf{n}'(\mathbf{r}') = \sqrt{\epsilon'(\mathbf{r}') \cdot \mu'(\mathbf{r}')}$ , experiencing an identical evolution in the spaces  $\mathbf{r}$  and  $\mathbf{r}'$ . For any response pair  $n(\mathbf{r})$  and  $n'(\mathbf{r}')$  created via  $\Omega(\mathbf{r})$ , transformation optics guarantees the causality of the resulting material in both spaces  $\mathbf{r}$  and  $\mathbf{r}'$  (see Methods for a detailed demonstration).

The main idea is to inverse design the geometrical deformation (eq 2) so that the transformed refractive index is that of a vacuum, with  $n'(\mathbf{r}') = 1$ :

$$\nabla\Omega \cdot \epsilon \cdot \nabla\Omega^\dagger \cdot \nabla\Omega \cdot \mu \cdot \nabla\Omega^\dagger = |\nabla\Omega|^2 \cdot 1 \quad (3)$$

When this special condition occurs, the transformed medium  $\mathbf{n}'(\mathbf{r}')$  appears as a deformed reflector immersed in a vacuum and the deformed surface defined from eq 2 acquires the ability to emulate the material with the user-defined refractive index  $n$  (Figure 1b,c).

Equation 3 comprises a system of nine nonlinear partial differential equations, to be solved for the unknown transformation  $\Omega(\mathbf{r})$  for a given desired material response in  $\epsilon(\mathbf{r})$  and  $\mu(\mathbf{r})$ . As a boundary condition, we assume that for  $\mathbf{r} \rightarrow \infty$  the transformation (eq 2) tends to the identity  $\Omega(\mathbf{r}) = \mathbf{r}$ , with  $\nabla\Omega = 1$ . This condition ensures that eq 3 represents physical materials localized in a finite area of space, while relaxing to a vacuum  $\epsilon(\mathbf{r}) = \mu(\mathbf{r}) = \mathbf{n}(\mathbf{r}) = 1$  in the far-field for  $\mathbf{r} \rightarrow \infty$ .

In this article, we begin to study the solution of eqs 3 for scalar dielectric or magnetic materials defined by a single quantity  $\epsilon(\mathbf{r}) \equiv \epsilon_{zz}(\mathbf{r})$  and  $\mu(\mathbf{r}) \equiv \mu_{zz}(\mathbf{r})$ , assumed without loss of generality on the  $z$  axis:

$$\epsilon = \begin{bmatrix} 1 & 0 \\ 0 & \epsilon(\mathbf{r}) \end{bmatrix}, \quad \mu = \begin{bmatrix} 1 & 0 \\ 0 & \mu(\mathbf{r}) \end{bmatrix} \quad (4)$$

The resulting refractive index  $\mathbf{n} = \sqrt{\epsilon \cdot \mu}$  acquires a traditional expression depending on a single scalar quantity  $n(\mathbf{r}) = \sqrt{\epsilon(\mathbf{r})\mu(\mathbf{r})}$ . Supplementary Note I shows that a necessary condition for the solution of eq 3 is that the deformation eq 2 is  $z$ -invariant with  $\nabla = [\nabla_\perp, 0]$  and  $\nabla_\perp = \left[ \frac{\partial}{\partial x}, \frac{\partial}{\partial y} \right]$ . In this condition, eq 3 reduces to

$$\begin{bmatrix} (\nabla_\perp \Omega_\perp \cdot \nabla_\perp \Omega_\perp^\dagger)^2 & 0 \\ 0 & n^2(\mathbf{r}) \end{bmatrix} = |\nabla_\perp \Omega_\perp^\dagger|^2 \cdot 1 \quad (5)$$

with  $\Omega_\perp = [x'(x, y), y'(x, y)]$ . Supplementary Note II shows that the solution to eq 5 is an inverse conformal mapping,<sup>28</sup> with  $\Omega = [\Re(\Omega), \Im(\Omega)]$  defined from the real  $\Re$  and imaginary  $\Im$  part of a single analytic function  $\Omega(u)$  of complex coordinate  $u = x + iy$  satisfying the scalar equation  $n^2(\mathbf{r}) = \left| \frac{d\Omega(u)}{du} \right|^2$ . We solve this problem with a pseudospectral approach<sup>29</sup> based on suitably

defined rational Chebyshev polynomials<sup>30</sup> in the complex domain. We expand the unknown deformation  $\Omega(u)$  as follows:

$$\Omega\left(\frac{u}{a}\right) = \frac{u}{a} + \beta_0 + \sum_{m=1}^{\infty} \beta_m T_m\left(\frac{u - ia}{u + ia}\right) \quad (6)$$

with  $T_m(v)$  being the Chebyshev polynomial of order  $m$ ,  $a$  being an arbitrary spatial scaling constant, and  $\beta_m$  being unknown coefficients. Chebyshev polynomials  $T_m(v)$  are a complete basis that represents any complex function on the unit circle  $-1 \leq |v| \leq 1$ .<sup>29</sup> In eq 6, we use a Cayley transform  $v = \frac{u - ia}{u + ia}$ <sup>31</sup> that maps the unit circle to the positive semi-infinite space  $y \geq 0$  and  $-\infty \leq x \leq \infty$ , providing a rational series expansion that represents any analytic function  $\Omega(u)$  in the complex domain. Additionally, we impose the condition  $\beta_0 = -\sum_{m=1}^{\infty} \beta_m$  to reduce eq 6 in the far-field to the identity transformation  $\Omega(u/a) = u/a$ , as the user can verify by direct substitution and as requested for the inverse solution of eq 3.

By expressing the derivative  $\frac{dT_m(u)}{du} = m \cdot U_{m-1}(u)$  with Chebyshev polynomials of second kind  $U_m$ , we obtain the nonlinear equation for the inverse design of the transformation  $\Omega(u)$ :

$$n^2\left(\frac{\mathbf{r}}{a}\right) = \left| 1 + \frac{2ia}{(u + ia)^2} \cdot \sum_{m=0}^{\infty} \beta_{m+1} (m + 1) \cdot U_m\left(\frac{u - ia}{u + ia}\right) \right|^2 \quad (7)$$

In the scalar limit of eq 4, the inverse design problem is equivalent to finding the set of coefficients  $\beta_m$  that satisfy eq 7 for a user-defined refractive index  $n(\mathbf{r})$  given at the input. Equation 7 is a nonlinear, second order equation in the coefficients  $\beta_m$ , and we here solved it by statistical learning via nonlinear regression.<sup>32</sup> Given a user-defined distribution of refractive index  $n(\mathbf{r})$ , we create a training data set composed of a discrete number  $n = 0, 1, \dots$  of refractive index values  $n(\mathbf{r}_n)$  sampled on a Chebyshev grid  $\mathbf{r}_n$ .<sup>29</sup> Each data set input–output couple  $[n(\mathbf{r}_n), \mathbf{r}_n]$ , when substituted in eq 7, originates a nonlinear equation for the regression coefficients  $\beta_{m+1}$ . These are calculated via nonlinear least-squares, by using a trust-region convex minimization routine.<sup>33</sup> After solving for the coefficients  $\beta_{m+1}$ , eq 6 predicts the deformation of coordinates  $\Omega(u)$  for any point  $\mathbf{r}'$  of the space and completes the solution of the problem.

In the family of materials designed via eq 7, the refractive index  $n(\mathbf{r})$  is solely defined from the spatial curvature of  $\Omega(u)$  arising from  $\left| \frac{d\Omega(u)}{du} \right|^2$ . As such,  $n(\mathbf{r})$  does not show any theoretical limit between zero and infinity, with accessible values limited to implementing the required curvature arising from the solution of eq 7.

### Nanoresonators with Ultrahigh Refractive Index

At visible frequencies, high refractive index available materials with  $n \leq 5$  are typically III–IV semiconductors including Ge, Si, GaAs, and GaSb.<sup>34</sup> In these media, it is traditionally challenging to exploit their highest values of the refractive index because of high losses,<sup>35,36</sup> and applications typically rely on  $3 \leq n \leq 4$ .<sup>3,37–45</sup> To the best of the authors' knowledge, the reported highest refractive index in the visible is  $n = 5.1$  for a block copolymer self-assembly metasurface.<sup>46</sup>

We here illustrate how it is possible via inverse design to engineer materials with ultrahigh refractive index ( $n \approx 100$ ), which do not exist at visible frequency, and user-defined profile. We set a Gaussian distribution of refractive index  $n(\mathbf{r})$  with amplitude  $n(\mathbf{r} = 0) = 100$  and planar width  $x/a = 0.1$ . Figure 2a



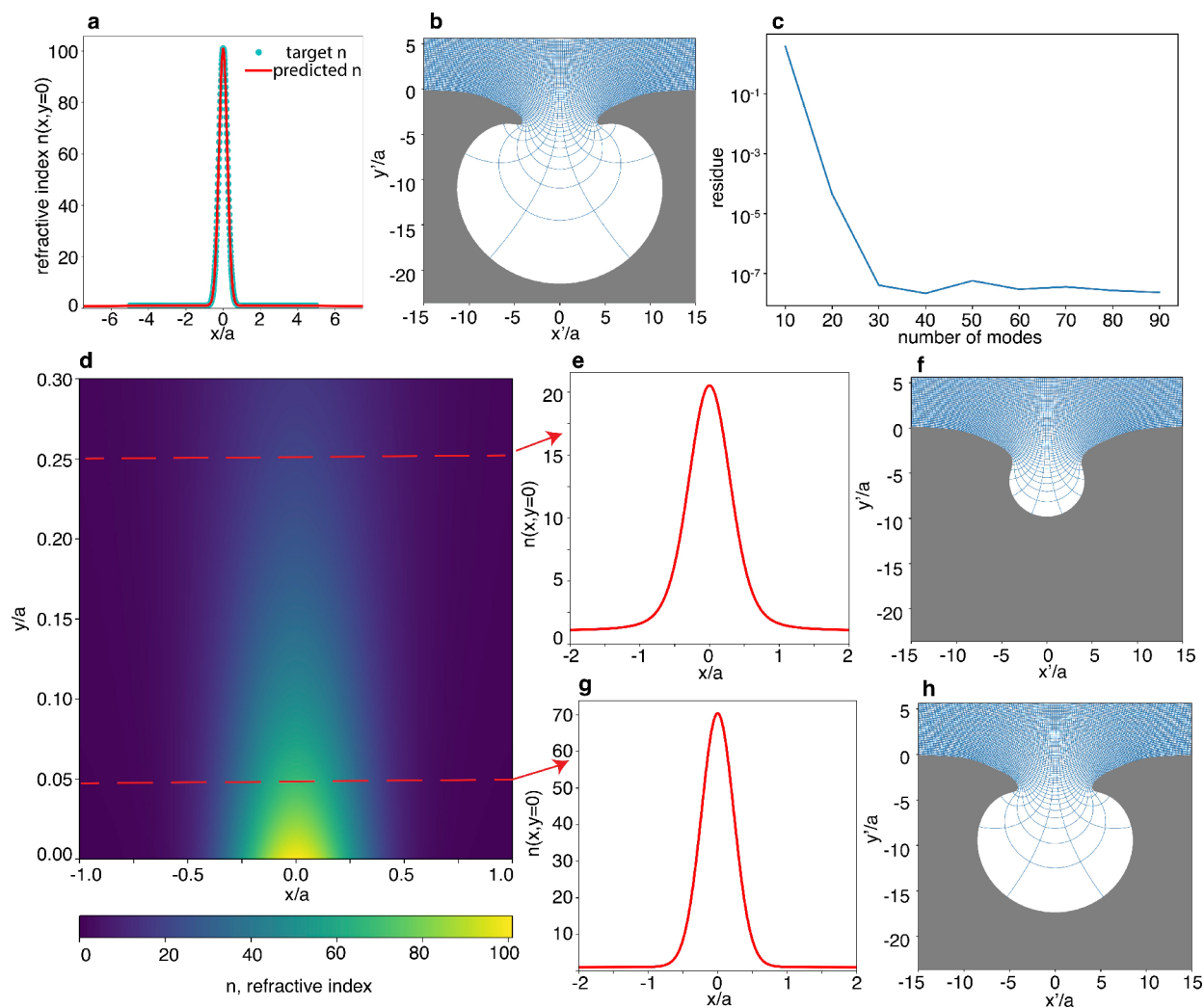


**Figure 2.** Ultrahigh refractive index nanoresonators. (a) Target refractive index profile (circle markers) and inverse design refractive index (solid red line). (b) Corresponding deformation in the accessible space. (c) Convergence of nonlinear regression for a varying number of modes  $M$ . (d) Spatial distribution of inverse designed refractive index in the design space. (e–g) Refractive index distribution with amplitudes  $n = 20$  and  $n = 70$ , respectively, and (f–h) corresponding deformations.

shows the corresponding training data set (cyan circle markers). In the solution of eq 6, we evaluate the minimum number  $M$  of coefficients  $\beta_{m+1}$  required to inverse solve the problem by increasing  $M$  and computing at each stage the prediction mean square error  $\text{MSE} = \|n(\mathbf{r}) - n_{\text{pred}}(\mathbf{r})\|$ , with  $n_{\text{pred}}(\mathbf{r})$  being the refractive index predicted from the transformation  $\Omega(u)$ . Figure 2c illustrates the convergence of MSE to the value of  $10^{-7}$  starting with  $M = 30$ . For this  $M$ , we compute a set of coefficients  $\beta_{m+1}$  which yields a solution for the predicted refractive index  $n_{\text{pred}}(\mathbf{r})$  values along the axis  $x$  matching the required Gaussian profile (Figure 2a solid red line). Figure 2d illustrates the refractive index distribution in the design space  $\mathbf{r}$ . The index relaxes exponentially in the  $y$ -axis, providing a diffusive-like nanoresonator profile with an ultrahigh refractive index region defined in a narrow length along  $y$ .

Figure 2b (solid gray area) shows the reflective deformation in the accessible space  $\mathbf{r}'$  that emulates the material with user-defined distribution of refractive index  $n(\mathbf{r})$  Figure 2a. The deformation corresponds to the mapping  $\mathbf{r}' = \Omega(\mathbf{r})$  for  $y = 0$  and  $-\infty < x < \infty$ . The solid blue lines in Figure 2b report the coordinate deformation in the remaining area of space for  $y \neq 0$ . A single coordinate transformation  $\Omega(u)$  defines an entire family

of materials with different distributions of refractive indices. If we consider a coordinate line at varying  $x$  and constant  $y_0$  in Figure 2d and set  $y_0$  as a new origin of coordinate along  $y$  via  $y \rightarrow y - y_0$ , this deformation generates a new reflective material in the accessible space  $\mathbf{r}$  with the index distribution defined by  $n(\mathbf{r})$  evaluated at the new origin  $y = 0$  and varying  $x$ . The corresponding refractive index maintains the same spatial profile along  $x$  but acquires a different amplitude due to the relaxation of the index values toward infinity (Figure 2d). Figure 2e–h illustrates this possibility, showing the engineering of different reflective deformations yielding Gaussian index profiles with maxima of  $n = 20$  and  $n = 70$ .

Supplementary Figure 1 illustrates examples of ultrahigh index resonators realized with different form factors. Panels a–c show the case of a flat-top resonator with a super-Gaussian spatial index profile. Supplementary Figure 1d–f shows the example of two adjacent resonators with different refractive indices, demonstrating the flexibility of this technique in designing complex index modulations that are not possible to observe at visible frequencies with conventional materials.

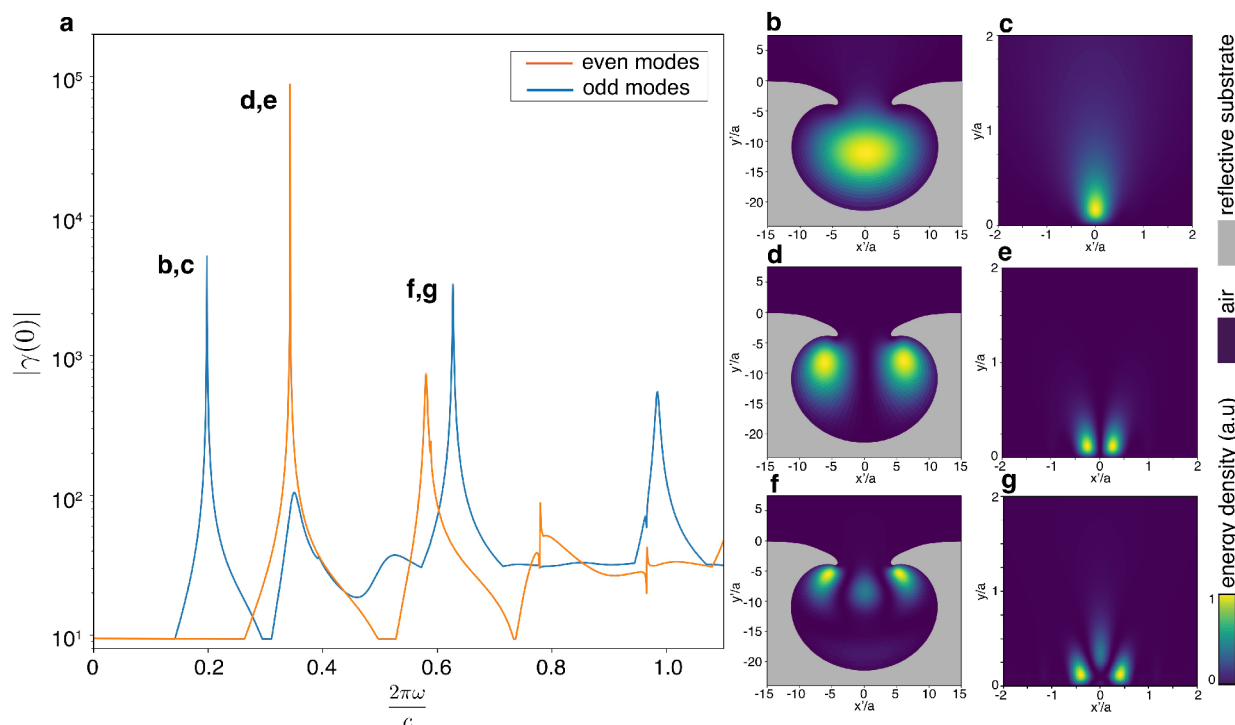


**Figure 3.** BIC states of inverse designed ultrahigh index resonators. (a) Eigenvalue amplitude  $|\gamma(0)|$  vs frequency  $k$ . (b–g) Electromagnetic energy spatial distribution for singular states in the accessible  $\mathbf{r}'$  and design  $\mathbf{r}$  spaces, respectively.

### Resonator Modes

Resonators designed by complex geometrical deformations support resonant states appearing as energy localization with frequency in the continuum of radiation modes. This result depends on the fact that, in the accessible space, there is nothing else than a deformed reflector immersed in a vacuum, and any mode should therefore appear as a bound state within a frequency range defined by the spectrum of continuum modes. Currently, research in the field of Bound States in the Continuum (BIC)<sup>47</sup> is attracting conspicuous interest because such radiationless modes open a wide manifold of applications for light management at the nanoscale. Contrary to reported BICs in conventional photonic structures, reflective meta-phonics allows access to a new family of BICs in which all the spatial localization of the electromagnetic radiation is physically accessible. We begin this analysis by studying singular resonances from the user-defined space  $\mathbf{r}$ , by decomposing the electric field  $\mathbf{E} = \mathbf{E}_t + \mathbf{E}_y$ , into a transverse  $\mathbf{E}_t$  component, lying on the  $(x, z)$  plane, and a normal contribution  $\mathbf{E}_y$ , along  $y$ . We then define the following eigenvalue problem for the transverse field:

$$\frac{\partial}{\partial y} \mathbf{E}_t(\mathbf{r}) = \gamma(y) \cdot \mathbf{E}_t(\mathbf{r}) \quad (8)$$

defining the spectral decomposition of the operator  $\frac{\partial}{\partial y}$  along the normal  $y$ -axis. Of particular interest are trapped modes arising from the singularities in the eigenvalue amplitude  $|\gamma(0)| \rightarrow \infty$  arising at  $y = 0$ . For the corresponding eigenvector  $\mathbf{E}_t(\mathbf{r})$  to be bounded and physical, the contribution  $\frac{\partial}{\partial y} \mathbf{E}_t$  is required to stay finite. This condition implies that  $\mathbf{E}_t \rightarrow 0$  at  $y = 0$ , satisfying the boundary condition  $\mathbf{E}_t = 0$  imposed by a perfect reflector over the entire  $(x, z)$  plane for transverse-electric (TE) polarized modes. Each singularity of eq 8 therefore defines a TE-polarized, nonradiating state that exists without any impinging source, by

autonomously satisfying the boundary conditions on the reflector plane at  $y = 0$ . The corresponding eigenvector  $\mathbf{E}_t(\mathbf{r})$  furnishes the spatial profile of the resulting TE-polarized BIC. As the singularity originating the BIC arises at  $y = 0$ , the electromagnetic field composing the BIC mode typically localizes in the proximity of the reflective plane at  $y = 0$ . In the accessible space  $\mathbf{r}'$ , such energy localizations appear in the vacuum-gaps areas created by geometric mapping  $\Omega(\mathbf{r})$  (Figure 1b). The case for TM polarization follows the same analysis, with the only difference of decomposing the magnetic field  $\mathbf{H} = \mathbf{H}_t + \mathbf{H}_y$  into transverse  $\mathbf{H}_t$  and normal  $\mathbf{H}_y$  contributions and formulating eq 8 for  $\mathbf{H}_t$ . The boundary condition of TM-polarized localizations,  $\mathbf{H}_t = 0$  at  $y = 0$ , implies that the energy maxima of these modes localize on the reflector surface. TE localizations, conversely, possess an electric field that completely localizes in the vacuum. This condition implies that this family of BICs allows the user to physically access all points of high energy localization, which offers a highly advantageous condition for implementing the vast spectrum of applications of BICs leveraging high energy localizations in space.<sup>47</sup>

We illustrate these results by solving the eigenvalue eq 8 with an approach that generalizes the work of.<sup>48</sup> The idea is to project the eigenvalue equation over a basis of scattering modes computed at  $\mathbf{r} \rightarrow \infty$ , and resolve the resulting discrete equations by a spectral method. Supplementary section III discusses the implementation details of this approach. Figure 3 illustrates calculation examples of BIC supported by the ultrahigh refractive index nanoresonator designed in Figure 2a. Figure 3a plots the corresponding eigenvalue amplitude  $|\gamma(0)|$  at  $y = 0$  for a varying frequency measured in wavevector units  $k = 2\pi\omega/c$ . As the resonator structure is symmetric in the  $(x, z)$  plane, we perform computations for even (solid blue lines) and odd (solid orange lines) BIC modes separately. The eigenvalue  $\gamma$  shows the formation of clear singular states with amplitudes reaching up to  $10^5$  at  $k = 0.3429$ . Each of these singularities defines a BIC state

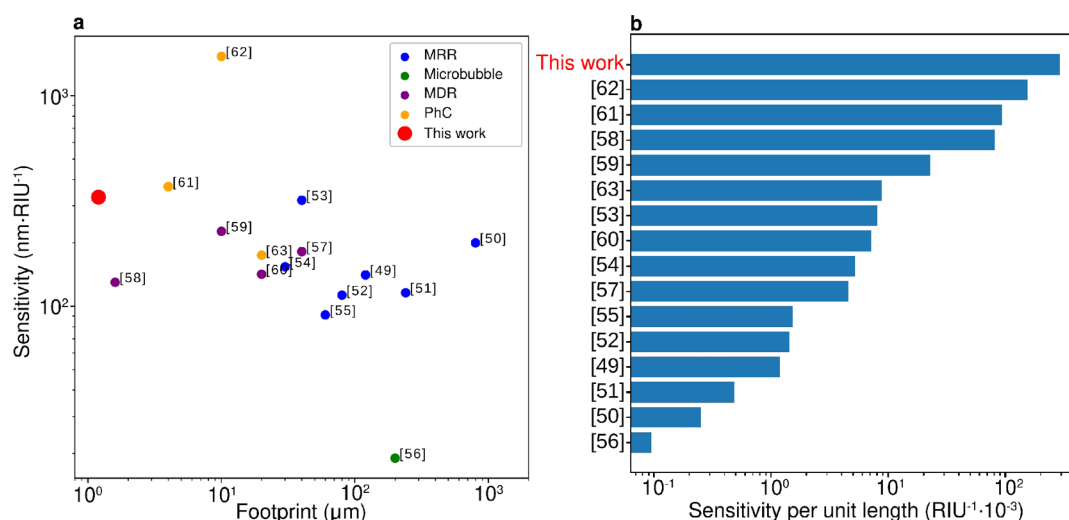


**Figure 4.** State-of-the-art in RI optical sensors. (a) Sensitivity vs sensor footprint. (b) Single figure of merit displaying the sensitivity per sensor footprint. MRR, microring resonator; MDR, microdisk resonator; PhC, photonic crystal; RIU, refractive index unit.

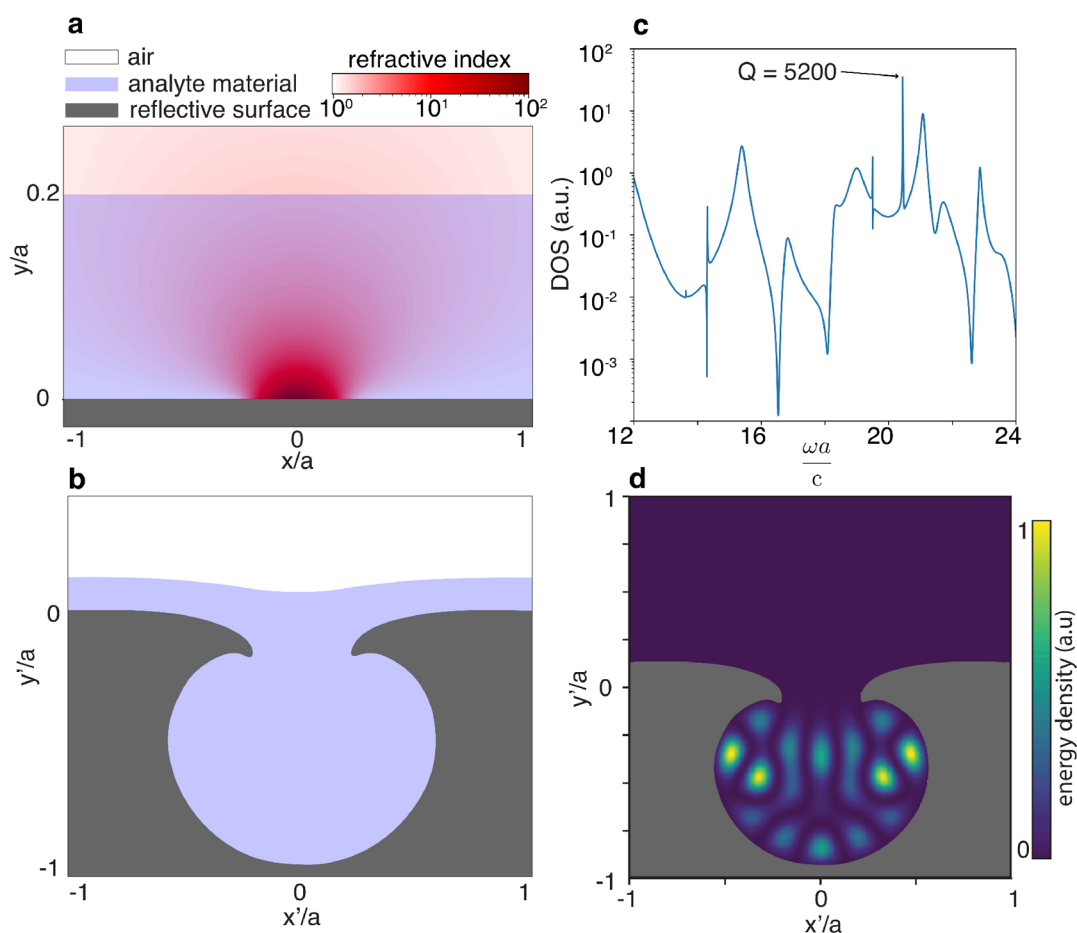


**Figure 5.** RI sensor based on inversely designed ultrahigh index material. (a) Sensor idea in the design space comprising a single resonator with ultrahigh refractive index region of  $n = 100$  confined above the substrate and an analyte placed on top of the substrate. (b) Corresponding configuration in the accessible space. (c) Density of states (DOS) of the resonator (solid blue line) with BIC states possessing  $Q = 5200$ . (d) Electromagnetic energy spatial distribution of the BIC state in the accessible space.

with a different energy profile. Figure 3b reports the spatial energy distribution in the accessible space, while panel c shows the corresponding profile in the design space. In the design space, odd and even TE polarized BIC modes confine electromagnetic energy inside the ultrahigh refractive region in

proximity to the reflective surface. In the accessible space, these modes manifest as narrow light localization in the vacuum gaps defined by the complex reflector spatial profile.

An advantage of this form of energy localization is the possibility to access the entire spatial distribution of high

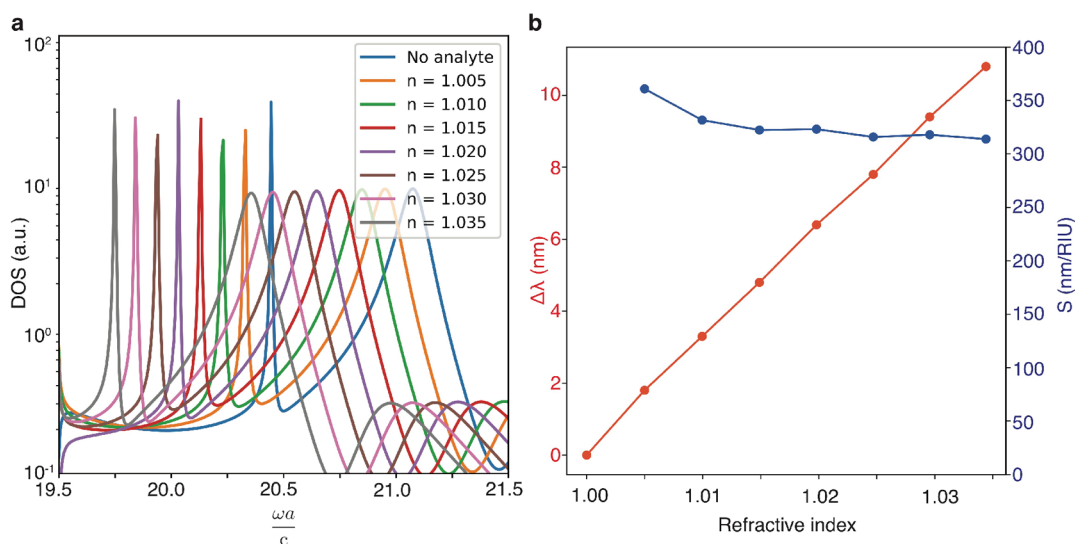


**Figure 6.** Performance of the RI sensing device. (a) Spectral shift of the BIC resonant wavelength for a varying refractive index  $n$  of the analyte. (b) Wavelength shift  $\Delta\lambda$  and differential sensitivity  $S$  vs refractive index change of the analyte.

refractive index, as observed from the mapping between the design and accessible spaces in Figure 3b-g. This property results from the user-defined refractive index region created by the surface profile of the deformed reflector, which provides trapping areas for singular states with a high degree of energy localization. In the next Section, we leverage this feature to design a new family of compact hypersensitive devices.

### Sensing Application

Figure 4a summarizes the state-of-the-art in refractive index (RI) sensing in sensitivity, measured in nm/RIU, vs sensor footprint, reported in units of micrometers.<sup>49–63</sup> Figure 4b orders these results in terms of a single FOM measuring the differential sensitivity per sensor path length, obtained as the ratio between the differential sensitivity and the sensor footprint. Sensors created with single resonator structures have typically lower performances than arrays of periodic structures such as, e.g., photonic crystals (PhC), which can reach sensitivities up to 1500 nm/RIU. Addressing sensor miniaturization without compromising performances is challenging: single resonator structures cannot benefit from nearest-neighbor constructive interactions and leverage only the quality-Q factor of the resonant modes supported by the refractive index of the resonator.

The sensor sensitivity depends strongly on a spatial overlap between the resonant mode's electric field and the volume occupied by the analyte.<sup>64</sup> To increase this interaction, the strategy is to place the analyte in the regions of near-field enhancement. However, in conventional sensors, enhanced fields are mostly confined within the resonator high index material, which is a portion of space physically inaccessible to the user. As a result of these shortcomings, sensitivities up to 300 nm/RIU require single resonators with large footprints of tens of microns.

The inverse design platform developed in this work can help address these issues by devising a system where the high refractive index region emulated by reflector deformation exists in the air space near the reflector's surface. In such a configuration, the analyte can physically access the high index region and probe the enhanced distribution of the electric field of the resonant mode. Such an enhanced interaction between

the BIC and the analyte leads to a significant frequency shift for more minor variations of analyte refractive index and, therefore, enhanced sensitivity.

Figure 5a,b illustrates the main design idea. We consider a single resonator in the design space possessing an ultrahigh refractive index of  $n = 100$  and Gaussian form factor, as shown in Figure 2c. The high refractive index region exists above the substrate in the air space (Figure 5a, red gradient area), and the analyte is on top of the substrate (Figure 5a, blue area). In this configuration, the analyte permeates the entire refractive index region, including the areas of  $n = 100$ . In the accessible space (Figure 5b), the structure appears as a deformed reflector with a conformal layer of material that fills up the cap space created by the modulated surface.

Figure 5c presents the density of states (DOS) of the resonator. We perform this calculation with Finite-Difference Time-Domain (FDTD) simulations with substrate material composed of Perfect Electric Conductor (PEC). We extract quality  $Q$  factors via a robust Prony method obtained by augmenting the original Prony scheme with statistical regression (see details in Methods). The structure supports diverse BIC states with quality factors up to  $Q = 5200$ , which we choose for our analysis. Quantitatively, this represents a performance increase of more than an order of magnitude than the state-of-art  $Q \sim 200$  reported by using a BIC in an all-dielectric single resonator of a similar footprint.<sup>3</sup> By setting the unit length  $a = 1 \mu\text{m}$ , the BIC with the highest quality factor occurs at the resonant wavelength of  $\lambda_{\text{BIC}} = 307 \text{ nm}$ , in the ultraviolet (UV) region. Figure 5d illustrates the spatial energy distribution of the BIC in the accessible space.

Beyond the ultrahigh value of the refractive index emulated by this deformed structure, a physical argument to understand the origin of such a high  $Q$ -factor value for the compact design comes from microwave electromagnetics. In this field, it is known that high refractive index materials, either with high permittivity or permeability, can be approximately modeled as thin layers possessing high admittance or impedance, respectively.<sup>65</sup> This condition, in turn, implies a resonant surface behavior in the transverse resonant eq 8, which provides an alternative demonstration that reflector cavities can trap equivalent electromagnetic energy to that of surfaces with high



permittivity or permeability. This approach can fine-tune the resonator coupling to the free space by modulating the surface with proper geometry, resulting in high Q-factor structures even in compact geometries. The BIC provides robust electromagnetic energy localization inside the deformed reflector, showing a complex distribution of multiple energy hot spots. In this sensor configuration, the analyte fills up the entire gap area (Figure 5b) and experiences a strong light-matter interaction by probing the high energy spots supported by the BIC state.

Figure 6 analyzes this mechanism in detail by computing the differential sensitivity from the wavelength shift of the BIC resonance. We computed these results from FDTD simulation by changing the refractive index of the analyte with steps  $\Delta n = 5 \times 10^{-3}$  RIU. Figure 6a reports the variation of the density of states for analytes with refractive indices between  $n = 1.005$  and  $n = 1.035$ . We do not observe any appreciable variation of the Q-factor. The system shows a perfect linear shift of the BIC resonant frequency (Figure 6b solid red line), while in conventional microdisk resonators with Q-factor reaching  $Q = 12\,000$  and footprints of few micrometers,<sup>58</sup> this value decreases to  $Q = 680$  in the presence of analytes, compromising the overall performances.

The resulting differential sensitivity stays between  $S = 350$  nm/RIU and  $S = 310$  nm/RIU, with an average value of  $S = 330$  nm/RIU (Figure 6b solid blue line). This design reports a record value of sensitivity per unit path length (Figure 4b), providing a single resonant structure with similar performances of periodic assembly of resonators with footprints of one order magnitude larger (Figure 4a).

## CONCLUSION

We have presented an inverse-design framework for implementing structures with user-defined nondispersive refractive indices and spatial form profiles in suitably deformed reflectors. We have discussed the basic optical circuitry, such as resonators with an ultrahigh refractive index of  $n = 100$  in diverse user-defined shapes. Leveraging the high refractive index response of these systems, we have designed a new class of hypersensitive sensors that demonstrate record values of differential sensitivity per unit path length  $S_{\text{pl}} = 290 \text{ nm} \cdot \mu\text{m}^{-1} \cdot \text{RIU}^{-1}$ .

The material platform discussed in this work can also open new experimental avenues in subwavelength light coupling in nanoscale waveguiding structures. The main idea is to perform the experimental setup studied in ref 42 and illustrated in Figure 4 of the paper. This work uses a nonradiating state excited by normal incident illumination to efficiently side-couple light energy in a strongly subwavelength dielectric waveguide. By designing a nonradiating BIC with a suitably deformed reflector and by choosing a subwavelength waveguide of core size comparable to the mode effective length of a surface plasmon polariton (SPP),<sup>12</sup> this technology could open to subwavelength light-guiding with similar transverse localization performances of SPP, and up to macroscopic ( $\approx \text{cm}$ ) propagation distances that are today unattainable by SPP.

Notably, such inverse metaphotonic reflectors can overcome two challenging problems. They allow us (i) to design structures with similar trapping performances to plasmonic structures but with no losses and (ii) to implement dielectric materials with user-defined refractive indices that go beyond the values available in physical materials. While these inverse-designed reflectors do not eliminate all issues, they replace physical limitations arising from points (i) and (ii) with a more

straightforward problem of engineering a surface with a user-implemented profile.

Experimentally, it is possible to implement reflector materials either in dielectrics or metallic structures. For dielectrics, broadband reflectors are realized via multilayer structures, either periodic or not, following the large available literature on the subject (see, e.g., ref 66 and references therein). Available metallic materials offer broadband reflecting properties across a broad spectrum of frequencies in the visible and near-infrared.<sup>12</sup> For the TE-polarized resonant BICs discussed in this work, material losses have minimal impact on the performances because the energy localization appears totally in the vacuum outside the reflector. Some existing nanofabrication techniques are already relevant to address these issues. While an exhaustive analysis is beyond the scope of this conceptual work, here we can mention two-photon lithography, which can already reach resolutions below the micrometer range<sup>67</sup> and is successively covered by a reflective layer, or powder bed fusion, which is essentially a version of three-dimensional printing for metallic structures.<sup>68</sup>

## METHODS

### Causality

We here prove that a material arising from the solution of eq 3 is physical and obeys the causality principle. Causality in optics is observed via Kramers–Kronig relationships,<sup>20</sup> which relate the real and imaginary part of the dielectric susceptibility  $\epsilon(\mathbf{r}, \omega) = \epsilon'(\mathbf{r}, \omega) + i\epsilon''(\mathbf{r}, \omega)$  and magnetic permeability  $\mu(\mathbf{r}, \omega) = \mu'(\mathbf{r}, \omega) + i\mu''(\mathbf{r}, \omega)$  expressed in the frequency domain  $\omega$ :

$$\sigma(\mathbf{r}, \omega) = \frac{1}{i\pi} \text{PV} \int_{-\infty}^{\infty} \frac{\sigma(\mathbf{r}, \omega')}{\omega' - \omega} d\omega' \quad (9)$$

with  $\sigma(\mathbf{r}, \omega) = \epsilon(\mathbf{r}, \omega)$  or  $\sigma(\mathbf{r}, \omega) = \mu(\mathbf{r}, \omega)$  and PV indicating the principal value. Multiplying eq 9 by  $\frac{\nabla\Omega^\dagger}{|\nabla\Omega^\dagger|^{1/2}}$  from the right and by  $\frac{\nabla\Omega}{|\nabla\Omega|^{1/2}}$  from the left, it becomes

$$\sigma'(\mathbf{r}', \omega) = \frac{1}{i\pi} \text{PV} \int_{-\infty}^{\infty} \frac{\nabla\Omega(\mathbf{r}) \cdot \sigma(\mathbf{r}, \omega) \cdot \nabla\Omega^\dagger(\mathbf{r})}{|\nabla\Omega^\dagger(\mathbf{r})| \cdot (\omega' - \omega)} d\omega' \quad (10)$$

which represents Kramers–Kronig relationships for the optical transformed material properties  $\sigma'(\mathbf{r}', \omega) = \epsilon'(\mathbf{r}', \omega)$ ,  $\mu'(\mathbf{r}', \omega)$  in the transformed physical coordinates  $\mathbf{r}' = \Omega(\mathbf{r})$ . As discussed in the previous section, the optical permittivity  $\epsilon = \epsilon(\mathbf{r})$  and permeability  $\mu = \mu(\mathbf{r})$  emulated via eq 3 are nondispersive and depend only on the spatial coordinates  $\mathbf{r}$ . Under this condition, the causality condition eq 10:

$$\begin{aligned} \sigma'(\mathbf{r}') &= \frac{\nabla\Omega(\mathbf{r}) \cdot \sigma(\mathbf{r}) \cdot \nabla\Omega^\dagger(\mathbf{r})}{|\nabla\Omega^\dagger(\mathbf{r})|} \cdot \text{PV} \int_{-\infty}^{\infty} \frac{d\omega'}{i\pi(\omega' - \omega)} \\ &= \frac{\nabla\Omega(\mathbf{r}) \cdot \sigma(\mathbf{r}) \cdot \nabla\Omega^\dagger(\mathbf{r})}{|\nabla\Omega^\dagger(\mathbf{r})|} \quad (11) \end{aligned}$$

reduces to transformation optics relationships of the material response, demonstrating that a material designed with this approach is perfectly causal. This result relies on the geometrical nature of transformation  $\Omega(\mathbf{r})$  used to create the material in eq 3, which does not depend on the frequency  $\omega$ . In this case,  $\text{PV} \int_{-\infty}^{\infty} \frac{1}{i\pi(\omega' - \omega)} d\omega' = 1$  and the real and imaginary part of eq 11 are decoupled, allowing to engineer a material that is fully causal.

### BIC Q-factor computations

We perform numerical simulations with our parallel NANOCPP FDTD solver. In the FDTD analysis, we studied the response of the structure on broadband TE-polarized light from the TFSF source by probing the electric field inside the nanoscale resonator and then by constructing the density of states (DOS). To resolve the Q-factor of



high- $Q$  modes within the DOS, we analyze the mode's energy decay by augmenting the Prony algorithm with a cross-validation model, as explained in the following. The Prony algorithm decomposes the signal into a sum of complex exponential:

$$\hat{f}(t) = \sum_{i=1}^M A_i e^{-\sigma_i t} \cos(\omega_i t + \phi_i) \quad (12)$$

with amplitudes  $A_i$ , decaying constants  $\sigma_i$ , frequencies  $\omega_i$ , and phases  $\phi_i$ . To compute these terms, we first divide the FDTD computed over time into two distinct sets: a training set from  $t = t_0$  to  $t = t_1$  and a testing set from  $t = t_1$  to the simulation time end  $t = t_2$ . We chose the intervals  $t_1 - t_0$  and  $t_2 - t_1$  to be approximately equal.

For a given input number of modes and sampling rate, we first solve linear prediction model for the training set with least-squares algorithm, find roots of a characteristic polynomial of the model, and then solve the original set of linear equations to obtain amplitudes and phases of an individual mode. Next, we apply this solution to the testing test and calculate the mean squared error between the FDTD data and the Prony model prediction. We then construct a surface of MSE values for different values of number of modes  $M$  and sampling rates  $T_s$  and select the values of  $M$  and  $T_s$  that yield the best prediction. For each mode, we then compute the  $Q$ -factors as

$$Q = \frac{\omega_i}{2\sigma_i} \quad (13)$$

## ■ ASSOCIATED CONTENT

### SI Supporting Information

The Supporting Information is available free of charge at <https://pubs.acs.org/doi/10.1021/acsnanoscienceau.2c00009>.

Necessary condition for the solution of eq 3, inverse conformal mapping solution for eq 5, solution for eigenvalue problem eq 8, ultrahigh index resonators with varying refractive index profiles, spectral decomposition of BIC modes supported by a high-index material (PDF)

## ■ AUTHOR INFORMATION

### Corresponding Author

Andrea Fratolocchi – PRIMALIGHT, Faculty of Electrical Engineering; Applied Mathematics and Computational Science, KAUST, Thuwal 23955-6900, Saudi Arabia; [orcid.org/0000-0001-6769-4439](https://orcid.org/0000-0001-6769-4439); Email: [andrea.fratolocchi@kaust.edu.sa](mailto:andrea.fratolocchi@kaust.edu.sa); [www.primalight.org](http://www.primalight.org)

### Authors

Maxim Elizarov – PRIMALIGHT, Faculty of Electrical Engineering; Applied Mathematics and Computational Science, KAUST, Thuwal 23955-6900, Saudi Arabia  
Yuri S. Kivshar – Australian National University, Canberra, ACT 2601, Australia; ITMO University, St. Petersburg 197101, Russia; [orcid.org/0000-0002-3410-812X](https://orcid.org/0000-0002-3410-812X)

Complete contact information is available at:

<https://pubs.acs.org/doi/10.1021/acsnanoscienceau.2c00009>

### Notes

The authors declare no competing financial interest.

## ■ ACKNOWLEDGMENTS

The authors acknowledge the use of resources of the Supercomputing Laboratory at KAUST. Y.K. acknowledges a

support from the Australian Research Council (Grant DP210101292), Russian Science Foundation (Grant 21-72-30018), and the U.S. Army International Office (Grant FA520921P0034).

## ■ REFERENCES

- Lee, J. S.; Park, J. Y.; Kim, Y. J.; Jeon, S.; Ouellette, O.; Sargent, E. H.; Kim, D. H.; Hyun, J. K. Ultrahigh resolution and color gamut with scattering-reducing transmissive pixels. *Nat. Commun.* **2019**, *10*, 4782.
- Koshelev, K.; Favraud, G.; Bogdanov, A.; Kivshar, Y.; Fratolocchi, A. Nonradiating photonics with resonant dielectric nanostructures. *Nanophotonics* **2019**, *8* (5), 725–745.
- Koshelev, K.; Kruk, S.; Melik-Gaykazyan, E.; Choi, J.-H.; Bogdanov, A.; Park, H.-G.; Kivshar, Y. Subwavelength dielectric resonators for nonlinear nanophotonics. *Science* **2020**, *367* (6475), 288–292.
- Wu, M.; Ding, L.; Sabatini, R. P.; Sagar, L. K.; Bappi, G.; Paniagua-Dominguez, R.; Sargent, E. H.; Kuznetsov, A. I. Bound state in the continuum in nanoantenna-coupled slab waveguide enables low-threshold quantum-dot lasing. *Nano Lett.* **2021**, *21* (22), 9754.
- Hüttenhofer, L.; Tittel, A.; Kuhner, L.; Cortes, E.; Maier, S. A. Anapole-assisted absorption engineering in arrays of coupled amorphous gallium phosphide nanodisks. *ACS Photonics* **2021**, *8* (5), 1469–1476.
- Wang, J.; Kuhne, J.; Karamanos, T.; Rockstuhl, C.; Maier, S. A.; Tittel, A. All-dielectric crescent metasurface sensor driven by bound states in the continuum. *Adv. Funct. Mater.* **2021**, *31* (46), 2104652.
- Nasir, M. E.; Krasavin, A. V.; Córdova-Castro, R. M.; McPolin, C. P. T.; Bouillard, J.-S. G.; Wang, P.; Zayats, A. V. Mode engineering in large arrays of coupled plasmonic–dielectric nanoantennas. *Adv. Opt. Mater.* **2021**, *9* (11), 2001467.
- Smirnova, D.; Leykam, D.; Chong, Y.; Kivshar, Y. Nonlinear topological photonics. *Appl. Phys. Rev.* **2020**, *7* (2), 021306.
- Chen, Y.; Lan, Z.; Li, J.; Zhu, J. Topologically protected second harmonic generation via doubly resonant high-order photonic modes. *Phys. Rev. B* **2021**, *104* (15), 155421.
- Fuechsle, M.; Miwa, J. A.; Mahapatra, S.; Ryu, H.; Lee, S.; Warschkow, O.; Hollenberg, L. C. L.; Klimeck, G.; Simmons, M. Y. A single-atom transistor. *Nat. Nanotechnol.* **2012**, *7*, 242–246.
- Desai, S. B.; Madhvapathy, S. R.; Sachid, A. B.; Llinas, J. P.; Wang, Q.; Ahn, G. H.; Pitner, G.; Kim, M. J.; Bokor, J.; Hu, C.; Wong, H.-S. P.; Javey, A.  $\text{MoS}_2$  transistors with 1-nanometer gate lengths. *Science* **2016**, *354*, 99–102.
- Maier, S.A. *Plasmonics: Fundamentals and Applications*; Springer: London, 2007.
- Huang, J.; Liu, C.; Zhu, Y.; Masala, S.; Alarousu, E.; Han, Y.; Fratolocchi, A. Harnessing structural darkness in the visible and infrared wavelengths for a new source of light. *Nat. Nanotechnol.* **2016**, *11*, 60–66.
- Huang, Y.-F.; Chattopadhyay, S.; Jen, Y.-J.; Peng, C.-Y.; Liu, T.-A.; Hsu, Y.-K.; Pan, C.-L.; Lo, H.-C.; Hsu, C.-H.; Chang, Y.-H.; Lee, C.-S.; Chen, K.-H.; Chen, L.-C. Improved broadband and quasi-omnidirectional anti-reflection properties with biomimetic silicon nanostructures. *Nat. Nanotechnol.* **2007**, *2*, 770–774.
- Koshelev, K.; Kivshar, Y. Dielectric resonant metapotonics. *ACS Photonics* **2021**, *8* (1), 102–112.
- Won, R. Into the ‘mie-tronic’ era. *Nat. Photonics* **2019**, *13*, 585–587.
- Shen, X.; Jun Cui, T. Planar plasmonic metamaterial on a thin film with nearly zero thickness. *Appl. Phys. Lett.* **2013**, *102* (21), 211909.
- Bonache, J.; Zamora, G.; Paredes, F.; Zuffanelli, S.; Aguilá, P.; Martín, F. Controlling the electromagnetic field confinement with metamaterials. *Sci. Rep.* **2016**, *6*, 37739.
- Yermakov, O. Y.; Hurshkainen, A. A.; Dobrykh, D. A.; Kapitanova, P. V.; Iorsh, I. V.; Glybovski, S. B.; Bogdanov, A. A. Experimental observation of hybrid te-tm polarized surface waves

- supported by a hyperbolic metasurface. *Phys. Rev. B* **2018**, *98* (19), 195404.
- (20) Bohren, C. F.; Huffman, D. R. *Electromagnetic Theory*; John Wiley & Sons, Ltd., 2007.
- (21) Boyd, R. W. *Nonlinear Optics*, Third ed.; Academic Press, Inc., 2008.
- (22) Pendry, J. B.; Aubry, A.; Smith, D. R.; Maier, S. A. Transformation optics and subwavelength control of light. *Science* **2012**, *337* (6094), 549–552.
- (23) Felbacq, D.; Bouchitté, G. *Metamaterials Modelling and Design*; Pan Stanford: New York, 2017.
- (24) McCall, M.; Pendry, J. B.; Galdi, V.; Lai, Y.; Horsley, S. A. R.; Li, J.; Zhu, J.; Mitchell-Thomas, R. C.; Quevedo-Teruel, O.; Tassin, P.; Ginis, V.; Martini, E.; Minatti, G.; Maci, S.; Ebrahimpouri, M.; Hao, Y.; Kinsler, P.; Gratus, J.; Lukens, J. M.; Weiner, A. M.; Leonhardt, U.; Smolyaninov, I. I.; Smolyaninova, V. N.; Thompson, R. T.; Wegener, M.; Kadic, M.; Cummer, S. A. Roadmap on transformation optics. *J. Opt.* **2018**, *20* (6), 063001.
- (25) So, S.; Rho, J. Geometrically flat hyperlenses designed by transformation optics. *J. Phys. D: Appl. Phys.* **2019**, *52* (19), 194003.
- (26) Pillozzi, L.; Farrelly, F. A.; Marcucci, G.; Conti, C. Machine learning inverse problem for topological photonics. *Commun. Phys.* **2018**, *1* (1), 57.
- (27) So, S.; Badloe, T.; Noh, J.; Bravo-Abad, J.; Rho, J. Deep learning enabled inverse design in nanophotonics. *Nanophotonics* **2020**, *9* (5), 1041–1057.
- (28) Schinzinger, R.; Laura, P. A. A. *Conformal Mapping: Methods and Applications*; Elsevier, 1991.
- (29) Fornberg, B. *A Practical Guide to Pseudospectral Methods*; Cambridge Monographs on Applied and Computational Mathematics; Cambridge University Press, 1996.
- (30) Guo, B.-y.; Shen, J.; Wang, Z.-q. Chebyshev rational spectral and pseudospectral methods on a semi-infinite interval. *Int. J. Numer. Meth. Engng.* **2002**, *53* (1), 65–84.
- (31) Kreyszig, E.; Kreyszig, H.; Norminton, E. J. *Advanced Engineering Mathematics*, tenth ed.; Wiley, Hoboken, NJ, 2011.
- (32) Hastie, T.; Tibshirani, R.; Friedman, J. *The elements of statistical learning: data mining, inference and prediction*, 2 ed.; Springer, 2009.
- (33) Agarwal, S.; Mierle, K., et al. *Ceres Solver*, ver. 2.1. <http://ceres-solver.org> (accessed 2022-05-25).
- (34) Khurgin, J. B. Expanding the photonic palette: Exploring high index materials. *ACS Photonics* **2022**, *9* (3), 743–751.
- (35) Kasap, S.; Capper, P. *Springer handbook of electronic and photonic materials*; Springer, 2017.
- (36) Baranov, D. G.; Zuev, D. A.; Lepeshov, S. I.; Kotov, O. V.; Krasnok, A. E.; Evlyukhin, A. B.; Chichkov, B. N. All-dielectric nanophotonics: the quest for better materials and fabrication techniques. *Optica* **2017**, *4* (7), 814–825.
- (37) Miroshnichenko, A. E.; Evlyukhin, A. B.; Yu, Y. F.; Bakker, R. M.; Chipouline, A.; Kuznetsov, A. I.; Luk'yanchuk, B.; Chichkov, B. N.; Kivshar, Y. S. Nonradiating anapole modes in dielectric nanoparticles. *Nat. Commun.* **2015**, *6*, 8069.
- (38) Liu, S.; Keeler, G. A.; Reno, J. L.; Sinclair, M. B.; Brener, I. Iii—v semiconductor nanoresonators—a new strategy for passive, active, and nonlinear all-dielectric metamaterials. *Adv. Opt. Mater.* **2016**, *4* (10), 1457–1462.
- (39) Schmid, M. Review on light management by nanostructures in chalcopyrite solar cells. *Semicond. Sci. Technol.* **2017**, *32* (4), 043003.
- (40) Yang, Z.-J.; Jiang, R.; Zhuo, X.; Xie, Y.-M.; Wang, J.; Lin, H.-Q. Dielectric nanoresonators for light manipulation. *Phys. Rep.* **2017**, *701*, 1–50.
- (41) Rybin, M. V.; Koshelev, K. L.; Sadrieva, Z. F.; Samusev, K. B.; Bogdanov, A. A.; Limonov, M. F.; Kivshar, Y. S. High-*q* supercavity modes in subwavelength dielectric resonators. *Phys. Rev. Lett.* **2017**, *119*, 243901.
- (42) Totero Gongora, J. S.; Miroshnichenko, A. E.; Kivshar, Y. S.; Fratallocchi, A. Anapole nanolasers for mode-locking and ultrafast pulse generation. *Nat. Commun.* **2017**, *8*, 15535.
- (43) Melik-Gaykazyan, E.; Koshelev, K.; Choi, J.-H.; Kruk, S. S.; Bogdanov, A.; Park, H.-G.; Kivshar, Y. From fano to quasi-bic resonances in individual dielectric nanoantennas. *Nano Lett.* **2021**, *21* (4), 1765–1771.
- (44) Kivshar, Y. All-dielectric meta-optics and non-linear nanophotonics. *Natl. Sci. Rev.* **2018**, *5*, 144–158.
- (45) Zhizhchenko, A.; Syubaev, S.; Berestennikov, A.; Yulin, A. V.; Porfirev, A.; Pushkarev, A.; Shishkin, I.; Golokhvast, K.; Bogdanov, A. A.; Zakhidov, A. A.; Kuchmizhak, A. A.; Kivshar, Y. S.; Makarov, S. V.; et al. Single-mode lasing from imprinted halide-perovskite microdisks. *ACS Nano* **2019**, *13* (4), 4140–4147.
- (46) Kim, J. Y.; Kim, H.; Kim, B. H.; Chang, T.; Lim, J.; Jin, H. M.; Mun, J. H.; Choi, Y. J.; Chung, K.; Shin, J.; Fan, S.; Kim, S. O.; et al. Highly tunable refractive index visible-light metasurface from block copolymer self-assembly. *Nat. Commun.* **2016**, *7*, 12911.
- (47) Bogdanov, A. A.; Fratallocchi, A.; Kivshar, Y. The science of harnessing light's darkness. *Nanophotonics* **2021**, *10* (17), 4171–4173.
- (48) Pagneux, V. Multimodal admittance method in waveguides and singularity behavior at high frequencies. *Journal of Computational and Applied Mathematics* **2010**, *234* (6), 1834–1841. Eighth International Conference on Mathematical and Numerical Aspects of Waves (Waves 2007).
- (49) Yalcin, A.; Papat, K.C.; Aldridge, J.C.; Desai, T.A.; Hryniewicz, J.; Chbouki, N.; Little, B.E.; Oliver King, Van, V.; Sai Chu; Gill, D.; Anthes-Washburn, M.; Unlu, M.S.; Goldberg, B.B.; et al. Optical sensing of biomolecules using microring resonators. *IEEE J. Select. Topics Quantum Electron.* **2006**, *12* (1), 148–155.
- (50) Kim, G.-D.; Son, G.-S.; Lee, H.-S.; Kim, K.-D.; Lee, S.-S. Integrated photonic glucose biosensor using a vertically coupled microring resonator in polymers. *Opt. Commun.* **2008**, *281* (18), 4644–4647.
- (51) Girault, P.; Lorrain, N.; Poffo, L.; Guendouz, M.; Lemaitre, J.; Carre, C.; Gadonna, M.; Bosc, D.; Vignaud, G. Integrated polymer micro-ring resonators for optical sensing applications. *J. Appl. Phys.* **2015**, *117* (10), 104504.
- (52) Schmidt, S.; Flueckiger, J.; Wu, W. X.; Grist, S. M.; Fard, S. T.; Donzella, V.; Khumwan, P.; Thompson, E. R.; Wang, Q.; Kulik, P., et al. Improving the performance of silicon photonic rings, disks, and bragg gratings for use in label-free biosensing. In *Biosensing and Nanomedicine VII*; SPIE, 2014; Vol. 9166, p 91660M.
- (53) Liu, P.; Shi, Y. Simultaneous measurement of refractive index and temperature using a dual polarization ring. *Applied optics* **2016**, *55* (13), 3537–3541.
- (54) Wei, H.; Krishnaswamy, S. Direct laser writing polymer micro-resonators for refractive index sensors. *IEEE Photon. Technol. Lett.* **2016**, *28* (24), 2819–2822.
- (55) Goykhman, I.; Desiatov, B.; Levy, U. Ultrathin silicon nitride microring resonator for biophotonic applications at 970 nm wavelength. *Appl. Phys. Lett.* **2010**, *97* (8), 081108.
- (56) Tang, T.; Wu, X.; Liu, L.; Xu, L. Packaged optofluidic microbubble resonators for optical sensing. *Appl. Opt.* **2016**, *55* (2), 395–399.
- (57) Hu, J.; Carlie, N.; Feng, N.-N.; Petit, L.; Agarwal, A.; Richardson, K.; Kimerling, L. Planar waveguide-coupled, high-index-contrast, high-*q* resonators in chalcogenide glass for sensing. *Opt. Lett.* **2008**, *33* (21), 2500–2502.
- (58) Wang, X.; Guan, X.; Huang, Q.; Zheng, J.; Shi, Y.; Dai, D. Suspended ultra-small disk resonator on silicon for optical sensing. *Opt. Lett.* **2013**, *38* (24), 5405–5408.
- (59) Kim, Y.; Lee, H. On-chip label-free biosensing based on active whispering gallery mode resonators pumped by a light-emitting diode. *Opt. Express* **2019**, *27* (23), 34405–34415.
- (60) Grist, S. M.; Schmidt, S. A.; Flueckiger, J.; Donzella, V.; Shi, W.; Talebi Fard, S.; Kirk, J. T.; Ratner, D. M.; Cheung, K. C.; Chrostowski, L. Silicon photonic micro-disk resonators for label-free biosensing. *Opt. Express* **2013**, *21* (7), 7994–8006.
- (61) Hamed Mirsadeghi, S.; Schelew, E.; Young, J. F. Photonic crystal slot-microcavity circuit implemented in silicon-on-insulator: High *q*

operation in solvent without undercutting. *Appl. Phys. Lett.* **2013**, *102* (13), 131115.

(62) Di Falco, A.; O'faolain, L.; Krauss, T. F. Chemical sensing in slotted photonic crystal heterostructure cavities. *Applied physics letters* **2009**, *94* (6), 063503.

(63) Garcia-Ruperez, J.; Toccafondo, V.; Banuls, M. J.; Castello, J. G.; Griol, A.; Peransi-Llopis, S.; Maquieira, A. Label-free antibody detection using band edge fringes in soi planar photonic crystal waveguides in the slow-light regime. *Opt. Express* **2010**, *18* (23), 24276–24286.

(64) Zhang, Y.; Liu, W.; Li, Z.; Li, Z.; Cheng, H.; Chen, S.; Tian, J. High-quality-factor multiple fano resonances for refractive index sensing. *Optics letters* **2018**, *43* (8), 1842–1845.

(65) Senior, T. B. A.; Volakis, J. L. *Approximate Boundary Conditions in Electromagnetics. EngineeringPro collection*; The Institution of Engineering and Technology, 1995.

(66) Yeh, P. *Optical waves in layered media*; Wiley Series in Pure and Applied Optics; Wiley: New York, 1988.

(67) Geng, Q.; Wang, D.; Chen, P.; Chen, S.-C. Ultrafast multi-focus 3-d nano-fabrication based on two-photon polymerization. *Nat. Commun.* **2019**, *10*, 2179.

(68) Elder, B.; Neupane, R.; Tokita, E.; Ghosh, U.; Hales, S.; Kong, Y. L. Nanomaterial patterning in 3d printing. *Adv. Mater.* **2020**, *32* (17), 1907142.